

Heat transfer and fluid flow during keyhole mode laser welding of tantalum, Ti–6Al–4V, 304L stainless steel and vanadium

R Rai¹, J W Elmer², T A Palmer² and T DebRoy¹

¹ Department of Materials Science and Engineering, The Pennsylvania State University, University Park, PA 16802, USA

² Lawrence Livermore National Laboratory, Livermore, CA, USA

Received 22 May 2007, in final form 11 July 2007

Published 30 August 2007

Online at stacks.iop.org/JPhysD/40/5753

Abstract

Because of the complexity of several simultaneous physical processes, most heat transfer models of keyhole mode laser welding require some simplifications to make the calculations tractable. The simplifications often limit the applicability of each model to the specific materials systems for which the model is developed. In this work, a rigorous, yet computationally efficient, keyhole model is developed and tested on tantalum, Ti–6Al–4V, 304L stainless steel and vanadium. Unlike previous models, this one combines an existing model to calculate keyhole shape and size with numerical fluid flow and heat transfer calculations in the weld pool. The calculations of the keyhole profile involved a point-by-point heat balance at the keyhole walls considering multiple reflections of the laser beam in the vapour cavity. The equations of conservation of mass, momentum and energy are then solved in three dimensions assuming that the temperatures at the keyhole wall reach the boiling point of the different metals or alloys. A turbulence model based on Prandtl's mixing length hypothesis was used to estimate the effective viscosity and thermal conductivity in the liquid region. The calculated weld cross-sections agreed well with the experimental results for each metal and alloy system examined here. In each case, the weld pool geometry was affected by the thermal diffusivity, absorption coefficient, and the melting and boiling points, among the various physical properties of the alloy. The model was also used to better understand solidification phenomena and calculate the solidification parameters at the trailing edge of the weld pool. These calculations indicate that the solidification structure became less dendritic and coarser with decreasing weld velocities over the range of speeds investigated in this study. Overall, the keyhole weld model provides satisfactory simulations of the weld geometries and solidification sub-structures for diverse engineering metals and alloys.

(Some figures in this article are in colour only in the electronic version)

1. Introduction

Laser welding, with its high energy density, is widely used as a joining technique for a range of applications requiring both shallow and deep penetrations. The inherent flexibility of the laser welding process is derived from its ability to operate in both the conduction mode for shallow penetration and the keyhole mode for deep penetration applications. Energy

densities above 10^5 W cm^{-2} are required to form the keyhole, which is a deep and narrow vapour cavity that forms because of evaporation of alloying elements [1, 2]. The formation of the keyhole improves the energy efficiency of the welding process due to multiple reflections of the laser beam within the cavity. Because of the high energy density, a portion of the metal vapour becomes excited and ionized, resulting in the formation of an electrically neutral plasma consisting of metal

Table 1. A selection of steady state keyhole mode laser welding research.

Swift-Hook and Gick [4]	Analytical model involving a line source.
Andrews and Atthey [5]	Investigated hydrodynamic limit to keyhole penetration for stationary laser or very low welding speeds, assuming an infinite liquid pool, and estimated the effect of surface tension on penetration depth.
Klemens [6]	Assumed circular cavity with radius variation with depth, simplified fluid flow into flows in horizontal and vertical planes, explained constriction in cavity near the surface.
Mazumder and Steen [7]	Three-dimensional heat transfer considering complete absorption of laser in the keyhole. Fluid flow was ignored.
Dowden <i>et al</i> [8–10]	Calculated free surface elevation/depression from axial flow around a cylindrical keyhole of varying radius.
Wei <i>et al</i> [11]	Considered energy and force balance on keyhole wall to study keyhole shape and temperature distribution.
Kroos <i>et al</i> [12]	Assumed a cylindrical keyhole, with self-consistently adjusting radius and keyhole temperature.
Kaplan [14]	Predicted asymmetric keyhole shape for high welding speeds through energy balance at keyhole walls.
Sudnik <i>et al</i> [15]	Numerical model involving vapour channel and weld pool; fluid flow separated into horizontal and vertical flows.
Matsunawa and Semak [16]	Assumed that only the front keyhole wall is exposed to laser beam to study the keyhole dynamics.
Ye and Chen [20]	Assumed a cylindrical keyhole and solved dimensionless Navier-Stokes equation taking keyhole radius as the characteristic length.
Zhao and DebRoy [21]	Studied porosity in aluminium using a modified form of Kaplan's model.
Rai <i>et al</i> [22–24]	Combined energy balance based keyhole calculation with three-dimensional fluid flow for partial and full penetration welds.

vapours, electrons and excited neutral atoms and ions above the surface of the weld and within the resulting vapour cavity. Depending on its properties, the plasma may attenuate the laser beam power and modify the beam radius and divergence owing to absorption and scattering [3].

Numerical modelling studies of the keyhole laser welding process very often include simplifications to make the computations tractable [4–15]. In many cases the simplifications restrict the models to specific materials systems or welding conditions, such as the welding of high thermal conductivity materials like aluminium alloys. Models developed for the welding of aluminium alloys at moderate laser powers ignore fluid flow in the weld pool and consider only heat transfer by conduction, since convective heat transfer is not the dominant mechanism and temperature gradients at the weld pool surface do not lead to significant Marangoni convection. However, for many engineering alloys, convective heat transfer can be very important, restricting the application of this often used assumption to high thermal conductivity materials [6, 8–11, 14]. On the other hand, relaxation of such restrictive assumptions makes the computational task impractical, since the model must now consider a range of additional physical process. For example, the calculation of the keyhole geometry will require the tracking of various gas/liquid free surfaces and the resulting fluid flow in the both the molten weld pool and the two-phase solid and liquid regions surrounding it.

It is instructive to follow the previous work to appreciate both the complexity of the simultaneous physical processes involved in keyhole mode laser welding and how the solution of such a complex problem has evolved in recent decades (table 1). Swift-Hook and Gick [4] formulated an analytical model considering a line source going into the workpiece. Klemens [6] calculated keyhole radius by balancing vapour pressure in the cavity, the hydrostatic pressure and the surface tension. Mazumder and Steen [7] considered three-dimensional heat transfer but ignored the effect of fluid flow. Dowden *et al* [8–10] assumed a keyhole with circular horizontal sections of radius varying with depth.

Kroos *et al* [12] assumed a cylindrical keyhole concentric with the laser beam valid only for low welding speeds. Kaplan [14] predicted asymmetric keyhole shapes by energy balance on keyhole walls which enabled prediction of weld geometry for high welding speeds, but neglected fluid flow. Sudnik *et al* [15] approximated the 3D fluid flow in the weld pool with 2D flow in the horizontal and vertical sections. Mazumder *et al* [18, 19] calculated free surface evolution by tracking gas/fluid interface considering recoil pressure, fluid flow, and multiple reflections. Zhao *et al* [21] studied the effect of beam defocusing on keyhole porosity by considering three-dimensional conduction heat transfer. A genetic algorithm based optimization tool was used by Rai and DebRoy [22] to estimate absorption coefficient and the beam radius for the welding of an aluminium alloy. Recently, the development of a computationally efficient convective heat transfer model considering asymmetric keyhole geometry was reported [23]. The work was extended to systems with partial and full penetration welds [24].

In short, existing heat transfer models have been developed to understand the keyhole mode laser welding for specific welding conditions and individual materials systems. What is needed and not currently available is a well tested phenomenological model for the keyhole mode welding that can be used for welding a wide range of metals and alloys with widely different physical properties and under a variety of welding conditions. Here, we report development and testing of a rigorous phenomenological model that embodies sufficient complexity of the problem to make the model predictions reliable. This model uses an efficient solution methodology, which has been refined over decades of research in fusion welding problems, to allow problems to be solved within a realistic time frame.

The fluid flow and heat transfer model was used to calculate the temperature fields, flow velocities, weld geometries and solidification parameters for the keyhole mode laser welding of vanadium, Ti–6Al–4V, 304L stainless steel (SS), and tantalum. These metals and alloys differ significantly in density, 4420–15000 kg m⁻³, solid thermal conductivity,

Table 2. Summary of laser powers.

Machine power setting (W)	Measured output (W)	% loss
220	202	8.2
440	396	10.0
660	588	10.9
880	779	11.5
1100	973	11.5
1320	1160	12.1
1540	1340	13.0
1760	1550	11.9
1980	1770	10.6
2200	1980	10.0

20–55 W m⁻¹ K⁻¹, boiling point, 3100–5643 K, and other properties. Particular attention is paid to the effects of variations in welding power and travel speed. The model predictions of weld pool shape and size are then compared with the corresponding experimental results. The results obtained from the current model reasonably and efficiently predict the weld characteristics for a range of welding conditions and material properties by considering three-dimensional fluid flow in the weld pool, while avoiding the computationally intensive task of vapour–liquid interface tracking.

2. Experiments

The welds described in this paper were made using a Rofin Sinar DY-022 diode pumped continuous wave Nd:YAG laser at Lawrence Livermore National Laboratory (LLNL) [25]. This system includes a laser power supply with a maximum power output of 2200 W, and the laser beam is delivered from the power supply to a Class 1 laser workstation using a 30 m long 300 μm diameter fibre optic cable. Within the workstation, the beam passes through a set of 1:1 focusing optics, consisting of a 160 mm collimator and a 160 mm focal length lens. The actual power output of the laser system at the exit of the optics assembly was measured using a water-cooled Coherent power meter, which has a rated measurement accuracy of ±1% and a calibration uncertainty of ±2%. Table 2 compares the power levels measured at the exit of the laser optics to the range of machine settings using the 300 μm diameter fibre. Overall, the laser power measurements display losses of approximately 10% of the machine setting. For all the cases in this paper, power delivered to the workpiece has been reported rather than the machine settings.

Autogenous bead on plate laser welds, 50 mm in length, were made on flat plates of vanadium, Ti-6Al-4V, 304L stainless steel, and tantalum. The chemical compositions of the four materials are given in table 3. The sample thickness for each of these materials varied, from 3.2 mm for the vanadium samples, to 6 mm for the tantalum samples, to 9.5 mm for the 304L stainless steel and 12.7 mm for the Ti-6Al-4V samples. Table 4 also provides a summary of the workpiece dimensions for all the materials used. It should also be noted that unlike the samples used for the other materials examined here, the tantalum samples contain a machined step-shaped butt joint.

Table 3. Material composition.

	Element	Weight %
Vanadium	Si	0.034
	C	0.0052
	H	0.0004
	N	0.017
	O	0.01
Ta	Commercially pure	
304L SS	Cr	18.2
	Ni	8.6
	Mn	1.7
	Mo	0.47
	Co	0.14
	Cu	0.35
	Si	0.44
	C	0.02
	N	0.082
	P	0.03
	S	0.0004
	Fe	Balance
	Ti-6Al-4V	Al
V		4.02
C		0.01
H		0.0022
Fe		0.25
N		0.007
O		0.117
Ti		Balance

All welds were made at sharp focus, with the beam focus set at the surface of the weld sample. During welding, argon shielding gas was supplied through a 4 mm diameter nozzle with a gas pressure of 5.51×10^5 Pa placed approximately 25 mm from the laser beam impingement area. Welds in the 304L stainless steel, Ti-6Al-4V and tantalum samples are made with the laser beam oriented normal to the weld sample. In the welding of the vanadium samples, the laser head was tilted at an angle of 5° normal to the sample surface and towards the leading edge of the weld and along the direction of welding to avoid any damage to the laser optics from potential back-reflection.

The welding experiments performed on each material system have utilized different ranges of welding parameters, which are summarized in table 4. In the first set of experiments, the effects of changes in the input power, from approximately 615 W through 1980 W, at a constant travel speed have been analysed on the vanadium, 304L stainless steel and the Ti-6Al-4V samples. These travel speeds vary between 16.9 mm s⁻¹ for the Ti-6Al-4V samples, to 19.1 mm s⁻¹ for the 304L stainless steel samples, to 25.4 mm s⁻¹ for the vanadium samples. The second set of experiments compared the effects of changing travel speeds at a constant input power for both tantalum and 304L stainless steel samples. For the tantalum samples, the travel speeds varied between 0.85 and 12.7 mm s⁻¹ at fixed input power of 1900 W, while those for the 304L stainless steel varied between 6.4 and 16.9 mm s⁻¹ at a fixed input power of 1980 W.

After welding, a section of the weld comprising approximately 6.4 mm of the weld length was removed from a location near the middle of each weld. This sample was mounted in cross-section, polished and etched to reveal both the microstructure and the resulting weld fusion zone

Table 4. Welding conditions. All welds were made using a 300 μ m diameter fibre with argon shielding gas.

Material	Power (W)	Welding speed (mm s ⁻¹)	Weld Depth (mm)	Weld Depth (mm)
Vanadium 3.2 mm × 152.4 mm × 25.4 mm	664	25.4	0.91	1.12
	887		1.22	1.32
	1109		1.51	1.52
	1332		1.66	1.65
	1777		2.18	1.9
	1980		2.28	2.13
304 SS 9.5 mm × 152.4 mm × 25.4 mm	664	19.1	1.92	1.3
	887		2.31	1.66
	1109		2.64	1.79
	1332		2.81	1.79
	1554		3.1	1.93
	1777		3.41	2.22
Ti-6Al-4V 12.7 mm × 152.4 mm × 76.2 mm	1980	16.9	3.58	2.19
	615		1.623	1.854
	720		1.93	2.108
	783		2.057	2.184
	875		2.21	2.337
	980		2.464	2.464
	1055		2.54	2.642
	1234		2.692	2.743
Tantalum 6 mm × 150 mm × 25 mm	1400	0.85	3.023	2.896
	1900		2.9	4.4
			1.7	3.5
			2.54	3.7
			3.81	3.1
			6.4	2.6
			12.7	2.2
			2.0	2.2
304 SS 9.5 mm × 152.4 mm × 25.4 mm	1980	19.1	6.4	4.48
			8.5	4.08
			10.6	3.61
			12.7	3.3
			14.8	3.23
			16.9	3.1

boundary, which defines its shape and size. Each metal/alloy required a different etchant to reveal the microstructure effectively. The 304L stainless steel samples were etched with an electrolytic oxalic acid etch commonly used with stainless steels. Kroll's etchant was used to reveal the fusion zone boundary in the Ti-6Al-4V sample. An etchant composed of 20 mL ethylene glycol, 10 mL HNO₃ and 10 mL HF was used for the vanadium samples. Finally an aqueous chemical etchant consisting of 30 g of ammonium bifluoride, 20 mL water and 50 mL nitric acid was used on the tantalum samples.

A digital micrograph of each weld cross-section was taken using a conventional optical microscope. From this micrograph, the weld width at the top surface and the weld depth below the surface of the plate were measured using a commercially available image analysis software package (Adobe Photoshop 7.0). For each weld, measurements of the weld depth along the centreline of the weld cross-section and the weld width along the surface of the sample have been made.

3. Mathematical model

3.1. Calculation of keyhole profile

The welding process is assumed to be quasi-steady state with a flat top surface. The transient fluctuations of the keyhole have been neglected. The keyhole geometry is calculated

using a model that considers energy balance on liquid-vapour interface assuming boiling point at the keyhole walls and constant absorption coefficients for absorption of the laser by the material. Since the orientation of keyhole is almost vertical, the heat transfer takes place mainly along the horizontal plane. During calculation of the asymmetric geometry of the keyhole, all temperatures inside the keyhole were assigned the boiling point of the alloy for the identification of the keyhole. The boiling point of the alloy was taken to be a temperature where the sum total of the equilibrium vapour pressures of all alloying elements over the alloy added up to 1 atm. At each horizontal xy plane, the keyhole boundary was identified by both a minimum x value and a maximum x value for any y value. Since the model and its application are available in the literature [14,21], these are not described here. Salient features of the model are presented in appendix A. Data used for the calculation of keyhole geometry are listed in table 5.

3.2. Heat transfer in the weld pool

After calculating the keyhole profile, the fluid flow and heat transfer in the weld pool is modelled by solving the equations of conservation of mass, momentum and energy in three dimensions. The molten metal is assumed to be an incompressible, laminar and Newtonian fluid. The data used for calculation of fluid flow is listed in table 6. The liquid

Table 5. Data used for keyhole calculations.

Physical property	V	304L SS	Ti-6Al-4V	Ta
Boiling point (K) [26, 27]	3683	3100	3315	5643
Density of liquid at boiling point (kg m ⁻³) [26–29]	5200	5800	3780	15 000
Specific heat of liquid at boiling point (J kg ⁻¹ K) [26, 28, 30, 32, 48]	907	800	730	231
Thermal conductivity of liquid at boiling point (W m ⁻¹ K ⁻¹) [28, 33–36]	50	29	30	67
Absorption coefficient η	0.28	0.30	0.30	0.32
Focal length of lens (mm)	160	160	160	160
Heat of evaporation of (J kg ⁻¹) [26, 27]	8.98 × 10 ⁶ (Va)	6.52 × 10 ⁶ (Fe) 6.21 × 10 ⁶ (Cr)	1.03 × 10 ⁶ (Ti)	4.1 × 10 ⁶ (Ta)
Plasma attenuation coefficient (m ⁻¹)	100	100	100	100

Table 6. Data used for fluid flow calculations.

Physical property	V	304L SS	Ti-6Al-4V	Ta
Solidus temperature (K) [26, 38, 48]	2175	1697	1878	3288
Liquidus temperature (K) [26, 38, 48]	2175	1727	1928	3288
Density of liquid (kg m ⁻³) [38]	5500	7000	4000	15 000
Specific heat of solid (J kg ⁻¹ K ⁻¹) [26, 38, 48]	730	712	610	190
Specific heat of liquid (J kg ⁻¹ K ⁻¹) [26, 28, 30, 32, 38]	780	800	700	231
Thermal conductivity of liquid (W m ⁻¹ K ⁻¹) [28, 33–36]	50	29	30	67
Thermal conductivity of solid (W m ⁻¹ K ⁻¹) [28, 33–36]	30	27	21	55
Viscosity (Pa s) [37, 38]	0.005	0.007	0.005	0.01
Coefficient of thermal expansion (1 K ⁻¹) [26]	1 × 10 ⁻⁵	1.96 × 10 ⁻⁵	8 × 10 ⁻⁶	6.6 × 10 ⁻⁶
Temperature coefficient of surface tension (N m ⁻¹ K ⁻¹) [26]	-0.31 × 10 ⁻³	-0.49 × 10 ⁻³	-0.26 × 10 ⁻³	-0.25 × 10 ⁻³
Enthalpy of solid at melting point (J kg ⁻¹) [26, 48]	1.25 × 10 ⁶	1.20 × 10 ⁶	1.12 × 10 ⁶	5.21 × 10 ⁵
Enthalpy of liquid at melting point (J kg ⁻¹) [26, 48]	1.58 × 10 ⁶	1.26 × 10 ⁶	1.49 × 10 ⁶	6.58 × 10 ⁵

metal flow in the weld pool can be represented by the following momentum conservation equation [39, 40]:

$$\rho \frac{\partial u_j}{\partial t} + \rho \frac{\partial(u_i u_j)}{\partial x_i} = \frac{\partial}{\partial x_i} \left(\mu \frac{\partial u_j}{\partial x_i} \right) + S_j, \quad (1)$$

where ρ is the density, t is the time, x_i is the distance along the i th ($i = 1, 2$ and 3) orthogonal direction, u_j is the velocity component along the j direction, μ is the effective viscosity and S_j is the source term for the j th momentum equation and is given as

$$S_j = -\frac{\partial p}{\partial x_j} + \frac{\partial}{\partial x_j} \left(\mu \frac{\partial u_j}{\partial x_j} \right) - C \left(\frac{(1 - f_L)^2}{f_L^3 + B} \right) u_j + \rho g \beta (T - T_{\text{ref}}) - \rho U \frac{\partial u_j}{\partial x_j}, \quad (2)$$

where p represents pressure, U is the welding velocity and β is the coefficient of volume expansion. The third term represents the frictional dissipation in the mushy zone according to the Carman–Kozeny equation for flow through a porous media [41, 42], where f_L is the liquid fraction, B is a very small computational constant introduced to avoid division by zero and C is a constant accounting for the mushy zone morphology (a value of 1.6×10^4 was used in the present study [42]). The fourth term is the buoyancy source term [43–47]. The last term accounts for the relative motion between the laser source and the workpiece [43].

The following continuity equation is solved in conjunction with the momentum equation to obtain the pressure field:

$$\frac{\partial(\rho u_i)}{\partial x_i} = 0. \quad (3)$$

In order to trace the weld pool liquid/solid interface, i.e. the phase change, the total enthalpy H is represented by a sum of sensible heat h and latent heat content ΔH i.e. $H = h + \Delta H$ [43]. The sensible heat h is expressed as $h = \int C_p dT$, where C_p is the specific heat and T is the temperature. The latent heat content ΔH is given as $\Delta H = f_L L$, where L is the latent heat of fusion. The liquid fraction f_L is assumed to vary linearly with temperature for simplicity [43]:

$$f_L = \begin{cases} 1 & T > T_L, \\ \frac{T - T_S}{T_L - T_S} & T_S \leq T \leq T_L, \\ 0 & T < T_S, \end{cases} \quad (4)$$

where T_L and T_S are the liquidus and solidus temperatures, respectively. Thus, the thermal energy transportation in the weld workpiece can be expressed by the following modified energy equation:

$$\rho \frac{\partial h}{\partial t} + \rho \frac{\partial(u_i h)}{\partial x_i} = \frac{\partial}{\partial x_i} \left(\frac{k}{C_p} \frac{\partial h}{\partial x_i} \right) + S_h, \quad (5)$$

where k is the thermal conductivity. The source term S_h is due to the latent heat content and is given as

$$S_h = -\rho \frac{\partial(\Delta H)}{\partial t} - \rho \frac{\partial(u_i \Delta H)}{\partial x_i} - \rho U \frac{\partial h}{\partial x_i} - \rho U \frac{\partial \Delta H}{\partial x_i}. \quad (6)$$

The heat transfer and fluid flow equations were solved for the complete workpiece. For the region inside the keyhole, the coefficients and source terms in the discretized algebraic equations were adjusted to obtain boiling point temperature and zero fluid velocities. The methodology for the implementation of known values of variables in any specified location of the solution domain is well documented in the literature [40].

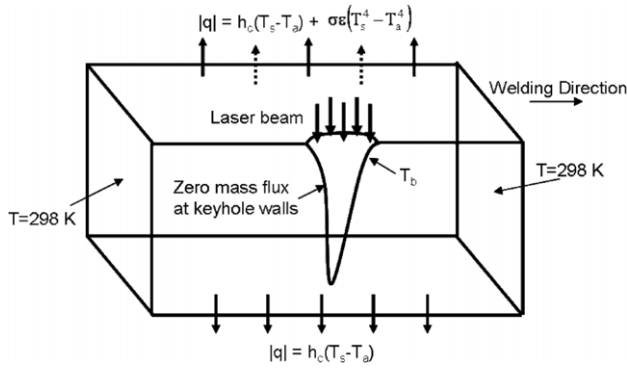


Figure 1. Boundary conditions.

3.2.1. Boundary conditions. A 3D Cartesian coordinate system is used in the calculation, and only half of the workpiece is considered since the weld is symmetrical about the weld centreline. A schematic of the boundary conditions is shown in figure 1. These boundary conditions are further discussed as follows.

Top surface. The weld top surface is assumed to be flat, except for the keyhole region. The velocity boundary condition is given as [48–52]

$$\begin{aligned} \mu \frac{\partial u}{\partial z} &= f_L \frac{d\gamma}{dT} \frac{\partial T}{\partial x}, \\ \mu \frac{\partial v}{\partial z} &= f_L \frac{d\gamma}{dT} \frac{\partial T}{\partial y}, \\ w &= 0, \end{aligned} \quad (7)$$

where u , v and w are the velocity components along the x , y and z directions, respectively, and $d\gamma/dT$ is the temperature coefficient of surface tension. As shown in this equation, the u and v velocities are determined from the Marangoni effect [48–52]. The w velocity is equal to zero since the outward flow at the pool top surface is assumed to be negligible.

The heat flux at the top surface is given as

$$k \frac{\partial T}{\partial z} \Big|_{\text{top}} = \frac{fQ\eta}{\pi r_b^2} \exp\left(-\frac{f(x^2 + y^2)}{r_b^2}\right) - \sigma \epsilon (T^4 - T_a^4) - h_c(T - T_a), \quad (8)$$

where r_b is the beam radius, f is the power distribution factor, Q is the total laser power, η is the absorptivity, σ is the Stefan–Boltzmann constant, h_c is the heat transfer coefficient and T_a is the ambient temperature. In equation (8), the first term on the right-hand side is the heat input from the Gaussian heat source. The second and third terms represent the heat loss by radiation and convection, respectively.

During welding, significant vaporization of the alloying elements results in a plume that contains metal vapour and plasma. As the laser beam passes through the plume, it is refracted and attenuated [53–57] through a combination of Rayleigh scattering, Rayleigh absorption, and inverse Bremsstrahlung mechanisms. The hot plasma also serves as a heat source for the workpiece. Thus, the effective heat source for the workpiece is slightly diffused and larger than the measured beam radius in the absence of a plume. The ‘effective’ value of the diameter of heat source is likely to depend on the welding conditions and the nature of the material

being welded. In the absence of any theoretical basis for estimation of the effect, a constant effective beam diameter was used in the calculations. The effective beam diameter of 0.4 mm was used here to represent the diffused beam emitted from the 0.3 mm diameter fibre and 1 : 1 focusing optics. This effective heat source diameter of 0.4 mm was used to represent the beam for all four materials studied in this investigation.

Symmetric plane. The boundary conditions are defined as zero flux across the symmetric surface, i.e. the vertical plane defined by the welding direction, as

$$\frac{\partial u}{\partial y} = 0, \quad v = 0, \quad \frac{\partial w}{\partial y} = 0, \quad (9)$$

$$\frac{\partial h}{\partial y} = 0. \quad (10)$$

Keyhole surface.

$$h = h_{\text{boil}}, \quad (11)$$

where h_{boil} is the sensible heat of the different materials at their respective boiling points. The velocity component perpendicular to keyhole surface is assigned zero to represent no mass flux due to convection.

Bottom surface. For partial penetration welds, a convective heat transfer boundary condition, with specified heat transfer coefficient, is specified at the bottom surface. Since the weld pool does not extend to the bottom, the velocities are zero at the bottom surface.

Solid surfaces. At all solid surfaces far away from the heat source, temperatures are set at ambient temperature (T_a) and the velocities are set to be zero.

3.3. Turbulence model

During keyhole mode laser welding, the rates of transport of heat, mass and momentum are often enhanced because of the presence of fluctuating velocities in the weld pool. The contribution of the fluctuating velocities is taken into account by using an appropriate turbulence model that provides a systematic framework for calculating effective viscosity and thermal conductivity [58, 59]. The values of these properties vary with the location in the weld pool and depend on the local characteristics of the fluid flow. In this work, a turbulence model based on Prandtl’s mixing length hypothesis is used to estimate the turbulent viscosity [58]:

$$\mu_t = \rho l_m v_t \quad (12)$$

where μ_t is the turbulent viscosity, l_m is the mixing length and v_t is the turbulence velocity. The mixing length at any location within the weld pool is the distance travelled by an eddy before its decay and is often taken as the distance from the nearest wall [59]. In a controlled numerical study of recirculating flows in a small square cavity, the extent of computed turbulent kinetic energy was found to be about 10% of the mean kinetic energy [60]. Yang and DebRoy [61] computed mean velocity and turbulent energy fields during GMA welding of HSLA 100 steel using a two equation k – ϵ model. Their results also show

that the turbulent kinetic energy was of the order of 10% of the mean kinetic energy. The turbulent velocity v_t can therefore be expressed as

$$v_t = \sqrt{0.1v^2}. \quad (13)$$

From equations (12) and (13), the following expression for the turbulent viscosity can be obtained

$$\mu_t = 0.3\rho l_m v. \quad (14)$$

Effective viscosity at a particular point is given as the sum of the turbulent (μ_t) and laminar (μ_l) viscosities, i.e. $\mu = \mu_t + \mu_l$. The corresponding local turbulent thermal conductivity, k_t , is calculated using the turbulent Prandtl number, which is defined in the following relationship:

$$Pr = \frac{\mu_t c_p}{k_t}. \quad (15)$$

For the calculations described here, the Prandtl number is set to a value of 0.9, based on previous modelling work [52, 59], and the turbulent thermal conductivity is then calculated.

3.4. Calculation methodology

The steps followed in the calculation of thermal and fluid flow fields are:

1. The keyhole geometry is obtained by local heat balance, available in the literature [14, 21]. The salient features of the calculation are described briefly in appendix A.
2. The computed keyhole geometry is identified during heat transfer and fluid flow calculations by assigning the boiling point to all grid points in the interior of the keyhole.
3. Momentum and energy balance equations, given by equations (1), (3) and (5), are solved assuming boiling temperature at the keyhole surface and no mass flux across it.
4. Viscosity and thermal conductivity values in the liquid phase are updated based on the turbulence model.
5. The liquid pool boundary is identified by the solidus isotherm during calculation.
6. Velocities and temperatures inside the keyhole are fixed at zero and boiling point, respectively, by adjusting appropriate coefficients in the discretized algebraic equations using the control volume technique. The fluid velocities at the keyhole surface adjust accordingly so that there is zero mass flux across the keyhole walls [40].

In the modelling of heat transfer and fluid flow during welding, it is important to consider absorption and scattering of the laser beam by the plasma/metal vapour plume. A detailed calculation of the spatially variable absorption is a laborious task since it involves calculation of materials flow and local electron densities in the plasma plume [56]. As a practical matter, in all previous modelling of heat transfer and fluid flow in keyhole mode laser welding calculations have been done with a constant absorption coefficient. This time tested methodology has been adapted here. (See appendix A.)

3.5. Computational time

A desktop computer with 3.2 GHz Pentium 4 processor and 1 GB RAM was used for the execution of the computer program. The computational time for convergence ranged between 7 and 20 min depending mainly on the grid size and the number of iterations. For example, for the welding of 304L stainless steel with 1980 W input power at 19.1 mm s⁻¹ welding speed, 1.09 million grid points (172 × 102 × 62) were used and 1500 iterations were necessary for convergence. The time taken for this run was 11 min 6 s. Since the momentum conservation equations are solved only in the weld pool region, the computational time depended not only on the total number of grid points and the number of iterations, but also on the size of the weld pool. The extent of imbalance of enthalpy and velocities in the computational domain was used to determine convergence. For example, when the absolute values of enthalpy imbalance divided by the enthalpy were added over all the enthalpy control volumes and the sum was less than 0.01%, enthalpy values were assumed to have converged. The same convergence criterion was used for each of the three velocity components.

4. Results and discussion

4.1. Weld pool geometry and fluid flow

Figure 2 shows the computed three-dimensional temperature contours and fluid flow patterns for 304L stainless steel, Ti-6Al-4V, vanadium, and tantalum for input laser power of 1900 W at a welding speed of 12.7 mm s⁻¹. Since surface tension depends on temperature, the large temperature gradients on the weld pool surface result in large surface tension gradients. As a result, liquid metal flows from near the keyhole to the edge of the weld pool owing to surface tension induced Marangoni convection, thereby enhancing the heat transfer. The radial heat transfer results in wider and longer weld pools. The velocities on the weld pool surface decay near the edge of the weld pool.

Depending on the extent of convective heat transfer and how it varies with depth, the weld pool may either have a spread near the top (as in figures 2(a)–(c)) or a cross-section with a gradual change in width from top to bottom (as in figure 2(d)). The three-dimensional views of weld pools in figure 2 show elongated weld pool shapes in the 304L stainless steel, Ti-6Al-4V alloy and vanadium samples as a result of the prominence of the Marangoni convection.

In the tantalum weld, shown in figure 2(d), the effect of Marangoni convection on the weld pool shape is less explicit. The high boiling point and density of tantalum results in lower weld penetration than other materials. In high thermal conductivity solids, efficient dissipation of heat from the weld pool into the solid region makes the weld pool relatively small. On the other hand, in low thermal conductivity materials, more heat is retained within the weld pool because of slow dissipation of heat into the solid region. As a result, the weld pool tends to be relatively large. High boiling and melting points, along with high thermal conductivity of solid tantalum result in relatively small weld pool depth and width compared with other materials under similar welding conditions (figure 2).

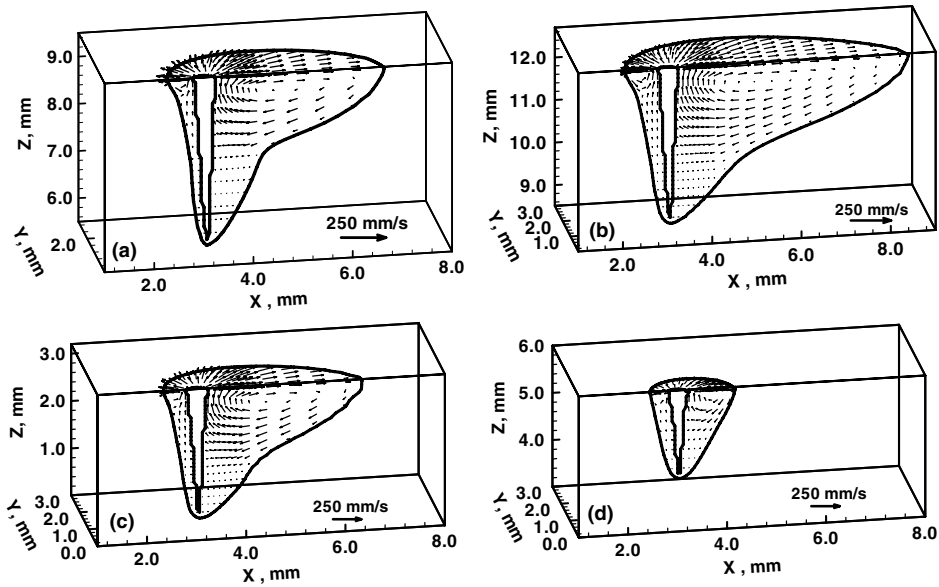


Figure 2. Three-dimensional weld pool shape and fluid flow for welds made with 1900 W laser power at 12.7 mm s⁻¹ welding speed. (a) 304L stainless steel, (b) Ti-6Al-4V, (c) vanadium and (d) tantalum.

Table 7. Peclet number for various welding systems.

Material	U (m s ⁻¹)	ρ (kg m ⁻³)	C_p (J kg ⁻¹ K ⁻¹)	L (m)	k (J m ⁻¹ s ⁻¹ K ⁻¹)	Thermal diffusivity (m ² s ⁻¹)	Pe
SS 304L	0.1	7000	800	0.001	29	5.18×10^{-6}	19.3
Ti-6Al-4V	0.1	4000	700	0.001	30	1.07×10^{-5}	9.3
V	0.1	5500	780	0.001	50	1.17×10^{-5}	8.6
Ta	0.1	15000	231	0.001	67	1.94×10^{-5}	5.1

The importance of convective heat transfer relative to conductive heat transfer can be determined by calculating the Peclet number, Pe , which is defined in the following relationship:

$$Pe = \frac{u\rho C_p L}{k}, \quad (16)$$

where u is the characteristic velocity, ρ is the density, C_p is the specific heat at constant pressure, L is the characteristic length, and k is the thermal conductivity. With a higher Peclet number, the contribution of convection to heat transfer is increased. It should be noted that the Peclet number varies with location within the weld pool. Thus, the high velocity region near the weld pool surface will have a higher Peclet number than the low velocity regions in the interior of the weld pool. Even in systems where convection is the dominant mechanism of heat transfer, the Peclet number values near a solid-liquid boundary will be very low due to small local fluid velocities. For a weld pool where conduction is the dominant heat transfer mechanism, the Peclet number values in most locations should be significantly lower than 1.

Table 7 lists the thermal diffusivity and Peclet numbers calculated for each material. Of the four materials, tantalum and 304L stainless steel display the highest and the lowest values of thermal diffusivity, respectively. The computed values of Pe show that convection is the main mechanism of heat transfer in the welding of all four materials. However, the ratio of heat transported by convection and conduction is highest for stainless steel and lowest for tantalum.

Figures 3–5 show the comparison of experimental and calculated weld cross-sections for different materials with variations of laser input power at fixed welding speeds. The dashed lines show the keyhole geometry as defined by the boiling points of various materials. The solid lines show the calculated weld pool boundary as defined by the solidus temperatures. The dotted lines mark the experimentally observed weld pool cross-sections. As shown in figure 3, there is good agreement between the calculated and experimental weld pool cross-sections of the 304L stainless steel welds for the three different input powers. The agreement seems to be better at lower input powers compared with higher powers. The calculated weld pool cross-sectional shape for Ti-6Al-4V agrees with the experimental weld pool shape as shown in figure 4. However, the weld pool dimensions agree better at lower heat input compared with higher heat input. For the vanadium welds shown in figure 5, the calculated weld cross-section agrees with the experimental cross-section. However, the calculations show less spread in the weld pool width at the top surface than experimentally observed. Figure 6–8 show a good agreement between the computed and experimental weld pool depths for the power variation study on 304L stainless steel, Ti-6Al-4V and vanadium welds.

Figures 9 and 10 show the comparison of experimental and calculated weld cross-sections for tantalum and 304L stainless steel welds made with fixed input power at different travel speeds. For tantalum welds shown in figure 9, the agreement between the experimental and calculated weld

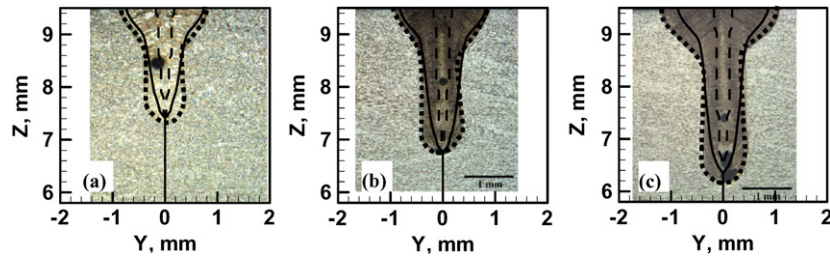


Figure 3. Comparison of calculated and experimental weld geometry for 304L stainless steel welds made at 19.1 mm s^{-1} welding speed with input laser powers (a) 887 W, (b) 1332 W and (c) 1777 W. The solid line represents the solidus and the dashed line represents the keyhole marked by boiling point temperature. The dotted line shows the experimentally observed weld pool boundary.

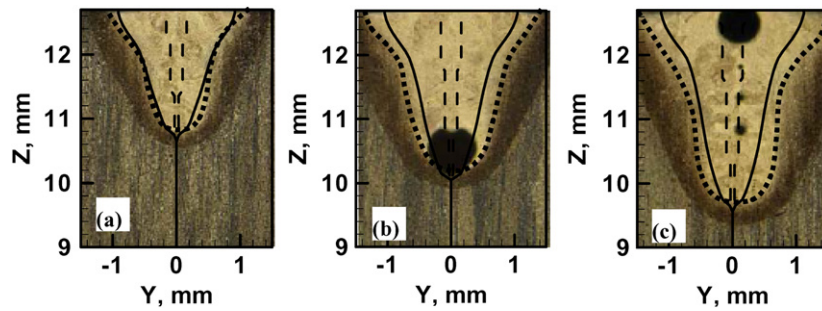


Figure 4. Comparison of calculated and experimental weld geometry for Ti-6Al-4V alloy welds made at 16.9 mm s^{-1} welding speed with input laser power (a) 720 W, (b) 1100 W, (c) 1400 W. The solid line represents the solidus and the dashed line represents the keyhole marked by boiling point temperature. The dotted line shows the experimentally observed weld pool boundary.

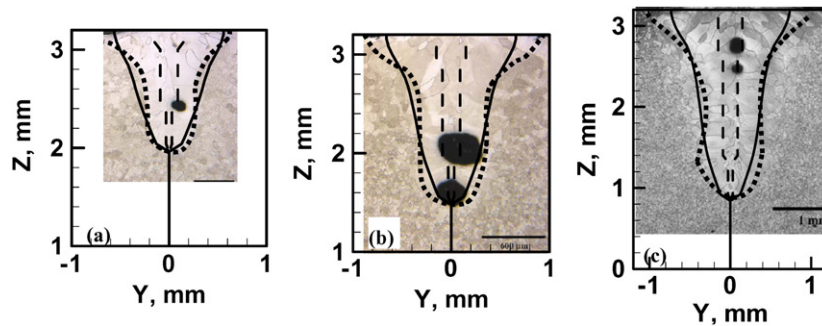


Figure 5. Comparison of calculated and experimental weld geometry for vanadium welds made at 25.4 mm s^{-1} welding speed with input laser powers (a) 887 W, (b) 1332 W and (c) 1777 W. The solid line represents the solidus and the dashed line represents the keyhole marked by boiling point temperature. The dotted line shows the experimentally observed weld pool boundary.

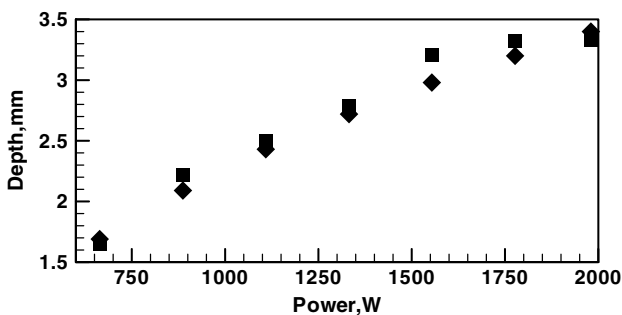


Figure 6. Experimental and calculated weld dimensions of 304L stainless steel welds made with different input laser powers at 19.1 mm s^{-1} welding speed. Square: experimental value, diamond: calculated value.

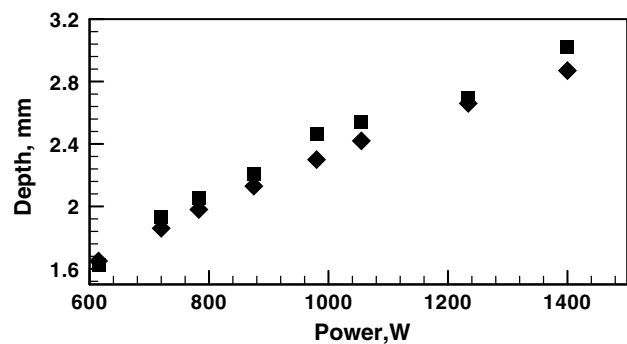


Figure 7. Experimental and calculated weld dimensions of Ti-6Al-4V alloy welds made with different input laser powers at 16.9 mm s^{-1} welding speed. Square: experimental value, diamond: calculated value.

pool cross-sections is better at higher welding speeds than at lower welding speeds. The experimental weld cross-sections, especially at lower welding speeds, exhibit a wide spread in the weld pool very close to the top surface. The calculated weld pool shapes, however, show only a gradual change in weld pool cross-sectional width with depth. The agreement between the calculated and experimental weld cross-sections for 304L stainless steel, shown in figure 10, is better at higher welding speeds, or at lower heat input per unit length. Figures 11 and 12 show good agreement between the computed and experimental weld pool depths for the welding

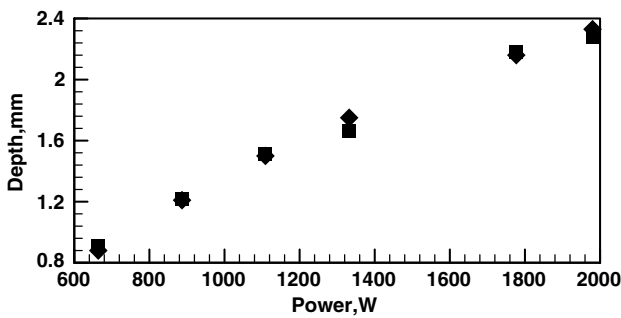


Figure 8. Experimental and calculated weld dimensions of vanadium welds made with different input laser powers at 25.4 mm s^{-1} welding speed. Square: experimental value, diamond: calculated value.

speed variation study on tantalum and 304L stainless steel, respectively.

The importance of convective heat transfer in the welding of the four materials is consistent with the corresponding thermal diffusivity values. That is, convection is very important for stainless steel with its low thermal diffusivity of $5.18 \times 10^{-6} \text{ m}^2 \text{ s}^{-1}$ and less important for tantalum with its high thermal diffusivity of $1.94 \times 10^{-5} \text{ m}^2 \text{ s}^{-1}$. A high value of temperature coefficient of surface tension for 304L stainless steel is also responsible for stronger convective heat transfer.

Different materials having considerably different physical properties like melting and boiling points, densities, and specific heat show different weld penetrations under similar welding conditions. High melting and boiling points, and high thermal diffusivity of tantalum result in small weld pools compared with other materials discussed here. The temperature coefficient of surface tension, melting/boiling point and thermal diffusivity among other material properties affect the weld pool shape. The difference of material properties like thermal diffusivity in the solid and the liquid states also affects the weld characteristics.

4.2. Solidification

With accurate calculations of the temperature and velocity fields, it is possible to use this knowledge to better understand other physical processes occurring during welding. For

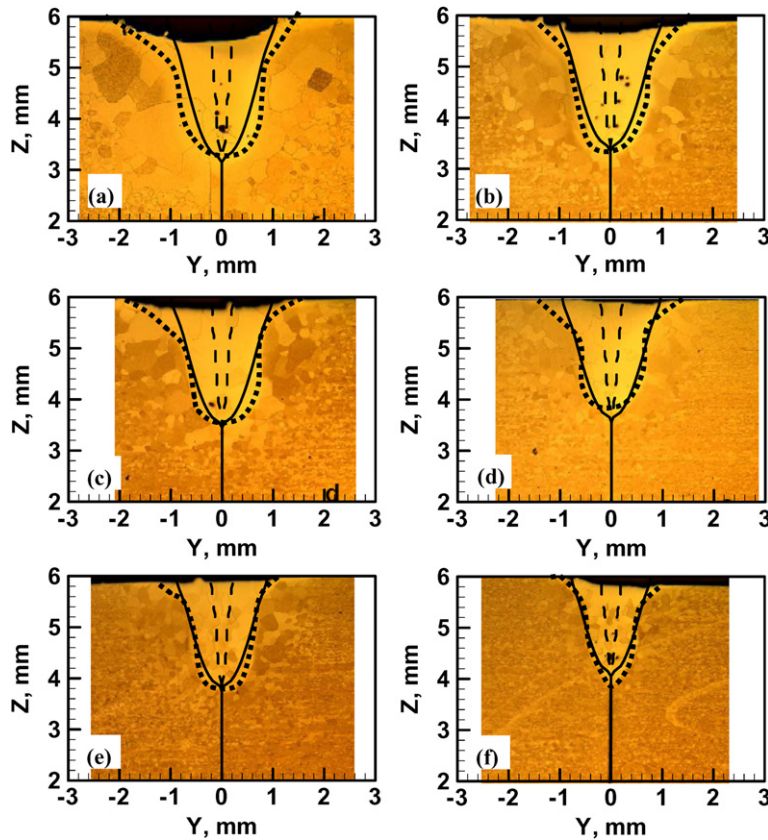


Figure 9. Comparison of calculated and experimental weld geometry for tantalum welds made with 1900 W input laser power at welding speeds (a) 0.85 mm s^{-1} , (b) 1.7 mm s^{-1} , (c) 2.54 mm s^{-1} , (d) 3.81 mm s^{-1} , (e) 6.4 mm s^{-1} and (f) 12.7 mm s^{-1} . The solid line represents the solidus and the dashed line represents the keyhole marked by boiling point temperature. The dotted line shows the experimentally observed weld pool boundary.

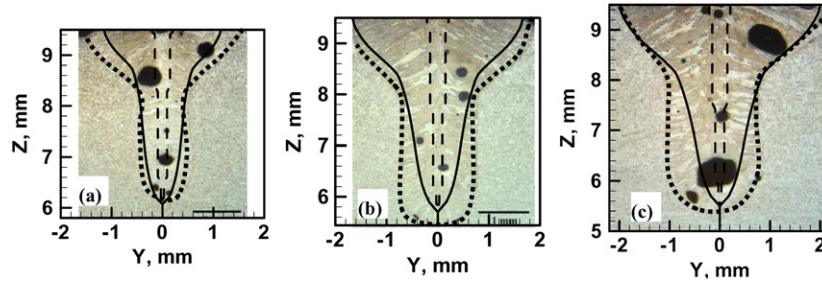


Figure 10. Comparison of calculated and experimental weld geometry for 304L stainless steel welds made with 1980 W input laser power at welding speeds (a) 16.9 mm s^{-1} , (b) 10.6 mm s^{-1} and (c) 8.5 mm s^{-1} . The solid line represents the solidus and the dashed line represents the keyhole marked by boiling point temperature. The dotted line shows the experimentally observed weld pool boundary.

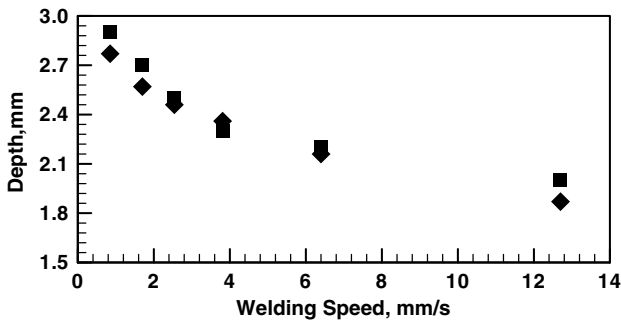


Figure 11. Experimental and calculated weld dimensions of tantalum welds made with 1900 W input laser power at different welding speeds. Square: experimental value, diamond: calculated value.

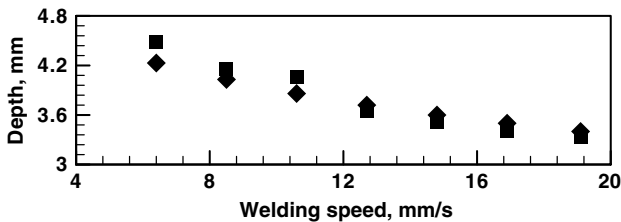


Figure 12. Experimental and calculated weld dimensions of 304L stainless steel welds made with 1980 W input laser power at different welding speeds. Square: experimental value, diamond: calculated value.

example, the solidification processes occurring in the different alloys studied here can be analysed. Solidification parameters like thermal gradient, G , solidification rate, R , undercooling, ΔT and alloy composition are often used to predict the solidification microstructure. The parameters G and R are used in combined forms G/R and GR to determine solidification morphology and scale of solidified microstructure. While G/R determines the solidification morphology, GR determines the scale of the solidification substructure. In this study no undercooling has been considered for simplicity. In steady state linear welding, the solidification rate is given as [48]

$$R = v \cos \beta, \quad (17)$$

where β is the angle between the welding direction and the normal at the solid-liquid boundary and v is the welding velocity. At the trailing edge of the weld pool, the solidification rate is equal to the welding velocity.

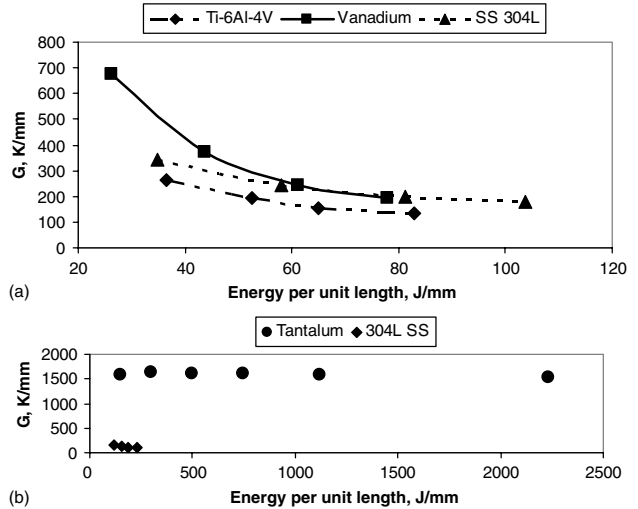


Figure 13. Temperature gradient versus heat input per unit length for (a) input power variation for vanadium, 304L stainless steel, Ti-6Al-4V alloy, (b) welding speed variation for tantalum and 304L stainless steel.

Figure 13(a) shows a plot of the computed variation of temperature gradient at the trailing edge of the weld pool, G , as a function of the heat input per unit length for the vanadium, 304L stainless steel, and Ti-6Al-4V alloy welds made at a constant welding speed and varying input laser powers. Figure 13(b) is a similar plot for tantalum and 304L stainless steel welds made with constant input laser powers but different welding speeds. For larger heat input per unit length, the weld pool length along the welding direction increases. Thus, the temperature drop from the boiling point of the material to its solidus temperature occurs over a larger length. Therefore, the temperature gradient decreases as the heat input per unit length increases for each of the materials. Due to the high melting and boiling points of tantalum and the shorter weld pool, the thermal gradient at the trailing edge of the weld pool was much higher for tantalum than for the other materials.

The G/R ratio can be used to understand the nature of solidification front. The criterion for plane front instability based on constitutional super-cooling is given by the following relation [1]:

$$G/R < \Delta T_E / D_L, \quad (18)$$

where ΔT_E represents the temperature difference between the solidus and liquidus temperatures of the alloy and D_L is the diffusivity of a solute in the liquid weld metal. Thus, $D_L <$

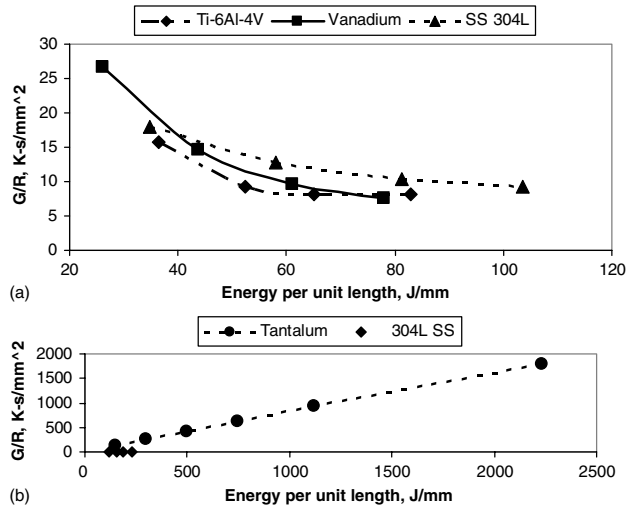


Figure 14. G/R versus heat input per unit length for (a) input power variation for vanadium, 304L stainless steel, Ti-6Al-4V alloy, (b) welding speed variation for tantalum and 304L stainless steel.

$\Delta T_E/(G/R)$, for plane front instability. Figure 14(a) shows the variation of G/R for varying input powers at constant welding speeds with vanadium, 304L SS and Ti-6Al-4V alloy. Figure 14(b) shows the variation of G/R for varying welding speeds at constant input powers for tantalum and 304L stainless steel. The G/R values are less than 20 K s mm⁻² for all cases of 304L stainless steel and Ti-6Al-4V alloys. The value of ΔT_E is 30 K for 304L stainless steel and 50 K for Ti-6Al-4V. Taking ΔT_E to be 40 K, $\Delta T_E/(G/R) = 2 \text{ mm}^2 \text{ s}^{-1} = 2 \times 10^{-6} \text{ m}^2 \text{ s}^{-1}$. Thus, if D_L is less than $2 \times 10^{-6} \text{ m}^2 \text{ s}$, plane front solidification will not occur. Since, for most liquid alloys, the diffusion coefficient is in the range 10^{-8} – $10^{-9} \text{ m}^2 \text{ s}^{-1}$ [62], the condition of plane front stability is not satisfied. For pure metals such as vanadium and tantalum, ΔT_E is equal to zero. Thus, constitutional super-cooling will not occur. In figures 14(a) and (b) the G/R trends have been plotted for metals, along with the alloys, for consistency.

Figure 15(a) shows the variation of GR for varying input powers at constant welding speeds for vanadium, stainless steel, and Ti-6Al-4V. Figure 15(b) is a similar plot for varying welding speeds at constant input powers for tantalum and 304L stainless steel. The value of GR , or the cooling rate at the trailing edge of the weld pool, decreases with the heat input per unit length, following the trend of G with constant welding speeds for each of the materials. The value of GR was slightly higher for vanadium welds as compared with Ti-6Al-4V alloy or 304L stainless steel because of the higher thermal conductivity of liquid vanadium and higher welding speed. Ti-6Al-4V alloy and 304L SS alloy with roughly the same thermal conductivity values and very close welding speeds have similar values for GR . Due to higher thermal conductivity of tantalum, the cooling rate is higher for tantalum compared with stainless steel for the same heat input per unit length, as shown in figure 15(b).

5. Summary and conclusions

A numerical model for keyhole mode laser welding was developed and tested to calculate fluid flow and heat transfer

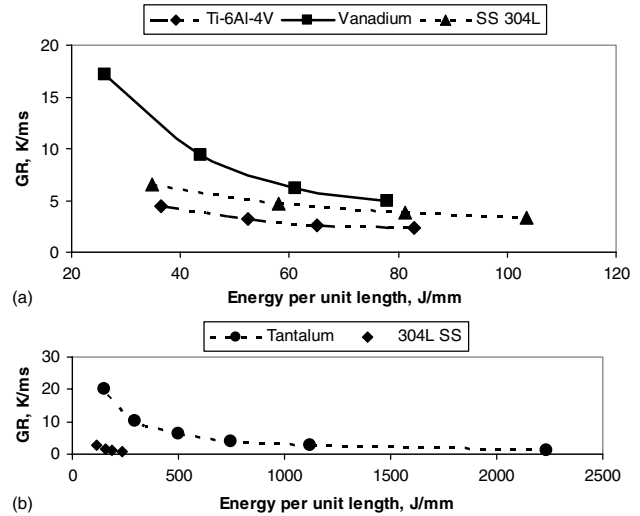


Figure 15. GR versus heat input per unit length for (a) input power variation for vanadium, 304L stainless steel, Ti-6Al-4V alloy, (b) welding speed variation for tantalum and 304L stainless steel.

during the laser welding of vanadium, tantalum, 304L stainless steel, and Ti-6Al-4V. The model was used to calculate the temperature and velocity fields, weld geometry and solidification parameters. A turbulence model based on Prandtl's mixing length hypothesis was used to estimate the effective viscosity and effective thermal conductivity values.

Convective heat transfer was the main mechanism of heat transfer for all four materials. The contribution of convection relative to conduction in the overall heat transfer was highest for 304L stainless steel and lowest for tantalum. The relative importance of these two mechanisms in the overall heat transfer depended on the thermal diffusivity and temperature coefficient of surface tension of the metals and alloys studied. Compared with 304L stainless steel, heat transfer by conduction was more significant for tantalum due to its high thermal diffusivity and lower temperature coefficient of surface tension. Thermophysical properties of the metals/alloys affected both the weld penetration and shape. These properties including the temperature coefficient of surface tension affected the weld pool shape through their influence on the heat transport process. The low thermal conductivity materials tended to have a fusion zone with a pronounced spread near the top. High boiling and melting points, and high solid state thermal diffusivity of tantalum resulted in smaller weld pools compared with the other materials studied. The solidification parameters calculated for 304L stainless steel and Ti-6Al-4V for the welding conditions considered here showed non-planar solidification front. The values of solidification parameters depend on the physical properties of the material.

The results show that a computationally efficient convective heat transfer model of keyhole mode laser welding, embodying a keyhole geometry sub-model and a methodology of convective heat transfer calculations perfected over decades in fusion welding, can significantly improve the current understanding of keyhole welding of different materials with widely different thermophysical properties.

Acknowledgments

The Pennsylvania State University portion of this work was supported by a grant from the US Department of Energy, Office of Basic Energy Sciences, Division of Materials Sciences, under grant number DE-FGO2-01ER45900. The LLNL portion of this work was performed under the auspices of the US Department of Energy, Lawrence Livermore National Laboratory, under Contract No W-7405-ENG-48. The authors also express gratitude to Bob Vallier and Jackson Go of LLNL for performing the optical metallography.

Appendix A. Calculation of keyhole geometry

A heat balance on the keyhole wall gives the following relation for local keyhole wall angle θ [21]:

$$\tan(\theta) = \frac{I_c}{I_a - I_v}, \quad (\text{A.1})$$

where I_c is the radial heat flux conducted into the keyhole wall, I_a is the locally absorbed beam energy and I_v is the evaporative heat flux on the keyhole wall. The value of I_c is obtained from a two-dimensional temperature field in an infinite plate with reference to a linear heat source. I_c is defined as

$$I_c(r, \varphi) = -\lambda \frac{\partial T(r, \varphi)}{\partial r}, \quad (\text{A.2})$$

where (r, φ) designates the location in the plate with the line source as the origin, T is the temperature and λ is the thermal conductivity. The two-dimensional temperature field can be calculated considering the conduction of heat from the keyhole wall into the infinite plate as [63]

$$T(r, \varphi) = T_a + \frac{P'}{2\pi\lambda} K_0(\Omega r) e^{-\Omega r \cos \varphi}, \quad (\text{A.3})$$

where T_a is the ambient temperature, P' is the power per unit depth, $K_0(\cdot)$ is the solution of the second kind and zero-order modified Bessel function and, $\Omega = \nu/(2\kappa)$, where ν is the welding speed and κ is the thermal diffusivity.

The locally absorbed beam energy flux, I_a , on the keyhole wall that accounts for the absorption during multiple reflections and the plasma absorption is calculated as [21]

$$I_a = e^{-\beta L} (1 - (1 - \alpha)^{1+\pi/4\theta}) I_0, \quad (\text{A.4})$$

where β is the plasma attenuation coefficient, L is the average path of the laser beam in plasma before it reaches the keyhole wall, α is the absorption coefficient of the workpiece, θ is the average angle between the keyhole wall and the initial incident beam axis, and I_0 is the local beam intensity which varies with depth from the surface and radial distance from the beam axis [21]. The keyhole profile is first calculated without considering multiple reflections. With the approximate keyhole dimensions, the average angle between the keyhole wall and incident beam axis is then calculated [21].

From Beer-Lambert law, $1 - e^{-\beta L}$ is the fraction of laser energy absorbed when the beam traverses a length L in the plasma [14]. For a value of 100 m^{-1} for the plasma attenuation coefficient, 5% of the laser beam is absorbed by the plasma for $L = 0.5 \text{ mm}$. For a value of 10 m^{-1} , and $L = 0.5 \text{ mm}$, 0.5% of the laser is absorbed by the plasma. Change in the plasma attenuation coefficient from 100 to 10 m^{-1} changes the calculated keyhole depth by less than 10%. Since the fluid flow

calculations are done by assuming a constant temperature on the keyhole walls, the effect of change in plasma attenuation coefficient on the fluid flow is only through a change in keyhole depth, which is not significant. Therefore, variations in this parameter do not significantly affect the heat transfer and fluid flow calculations.

Accurate values of the plasma attenuation coefficient for Nd-YAG laser for different metal vapours are not available in literature. Kaplan [14] used an average value of 100 m^{-1} for CO_2 laser welding of mild steel for inverse Bremsstrahlung mechanism. An attenuation coefficient of 7 m^{-1} was reported by Grees *et al* [53] for attenuation of Nd-YAG laser by Rayleigh scattering mechanism [3]. Laser beam is also absorbed by the plasma during multiple reflections within the keyhole. Considering all attenuation mechanisms, attenuation in the plasma above the weld surface, and attenuation during multiple reflections, a value of 100 m^{-1} has been taken for the modified attenuation coefficient.

$1 + (\pi/4\theta)$ in equation (A.4) represents the average number of reflections that a laser beam undergoes before leaving the keyhole [21]. When a laser beam of intensity I_0 traverses a length L in the plasma before reaching the material surface, $(1 - e^{-\beta L}) I_0$ is absorbed by the plasma. Of the remaining $e^{-\beta L} I_0$ which falls on the material, $(1 - \alpha) e^{-\beta L} I_0$ is reflected. After $1 + (\pi/4\theta)$ reflections, $(1 - \alpha)^{1+\pi/4\theta} e^{-\beta L} I_0$ of the intensity is reflected and the remaining $(1 - (1 - \alpha)^{1+\pi/4\theta}) e^{-\beta L} I_0$ is absorbed. For $\alpha = 0.3$ and $1 + (\pi/4\theta) = 6$, $L = 0.5 \text{ mm}$, about 5% of the local beam intensity is absorbed by the plasma, about 84% is absorbed by the material and the remaining 11% leaves the keyhole.

The evaporative heat flux, I_v on the keyhole wall is given as

$$I_v = \sum_{i=1}^n J_i \Delta H_i, \quad (\text{A.5})$$

where n is the total number of alloying elements in the alloy, ΔH_i is the heat of evaporation of element i , and J_i is the evaporation flux of element i given by the modified Langmuir equation [64-66].

$$J_i = \frac{a_i P_i^0}{7.5} \sqrt{\frac{M_i}{2\pi R T_b}}, \quad (\text{A.6})$$

where a_i is the activity of element i , P_i^0 is the equilibrium vapour pressure of element i over pure liquid at the boiling point T_b and M_i is the molecular weight of element i . The factor 7.5 is used to account for the diminished evaporation rate at 1 atm pressure compared with the vaporization rate in vacuum and is based on previous experimental results [64, 65].

References

- [1] DebRoy T and David S A 1995 *Rev. Mod. Phys.* **67** 85-116
- [2] David S A and DebRoy T 1992 *Science* **257** 497-502
- [3] Nonhof C J 1988 *Material Processing with Nd-YAG lasers* (Scotlan: Electrochemical, Ayz)
- [4] Swift-Hook D E and Gick A E F 1973 *Weld. J. (Miami)* **52** 492s-499s
- [5] Andrews J G and Atthey D R 1976 *J. Phys. D: Appl. Phys.* **9** 2181-94
- [6] Klemens P G 1976 *J. Appl. Phys.* **47** 2165-74
- [7] Mazumder J and Steen W M 1980 *J. Appl. Phys.* **51** 941-47

- [8] Dowden J, Davis M and Kapadia P 1983 *J. Fluid Mech.* **126** 123–46
- [9] Dowden J, Postacioglu N, Davis M and Kapadia P 1987 *J. Phys. D: Appl. Phys.* **20** 36–44
- [10] Postacioglu N, Kapadia P, Davis M and Dowden J 1987 *J. Phys. D: Appl. Phys.* **20** 340–5
- [11] Wei P S, Wu T H and Chow Y T 1990 *J. Heat Transfer* **112** 163–9
- [12] Kroos J, Gratzke U and Simon G 1993 *J. Phys. D: Appl. Phys.* **26** 474–80
- [13] Metzbowler E A 1993 *Metall. Trans. B* **24** 875–80
- [14] Kaplan A 1994 *J. Phys. D: Appl. Phys.* **27** 1805–14
- [15] Sudnik W, Radaj D and Erofeev W 1996 *J. Phys. D: Appl. Phys.* **29** 2811–17
- [16] Matsunawa A and Semak V 1997 *J. Phys. D: Appl. Phys.* **30** 798–809
- [17] Solana P and Ocana J L 1997 *J. Phys. D: Appl. Phys.* **30** 1300–13
- [18] Ki H, Mohanty P S and Mazumder J 2002 *Metall. Mater. Trans. A* **33A** 1817–30
- [19] Ki H, Mohanty P S and Mazumder J 2002 *Metall. Mater. Trans. A* **33A** 1831–42
- [20] Ye X H and Chen X 2002 *J. Phys. D: Appl. Phys.* **35** 1049–56
- [21] Zhao H and DebRoy T 2003 *J. Appl. Phys.* **93** 10089–96
- [22] Rai R and DebRoy T 2006 *J. Phys. D: Appl. Phys.* **39** 1257–66
- [23] Rai R, Roy G G and DebRoy T 2007 *J. Appl. Phys.* **101** 054909
- [24] Rai R, Kelly S M, Martukanitz R P and DebRoy T 2007 *Metall. Mater. Trans. A* submitted
- [25] Palmer T A, Elmer J W, Pong R and Gauthier M D 2004 Welding stainless steels and refractory metals using diode-pumped continuous wave Nd : YAG lasers *Lawrence Livermore National Laboratory Internal Report UCRL-TR-206885*
- [26] Brandes E A and Brook G B (ed) 1992 *Smithells Metals Reference Book* 7th edn (Oxford: Butterworth Heinemann)
- [27] Lide D R (ed) 2000 *CRC Book of Chemistry and Physics* 81st edn (Boca Raton, FL: CRC Press)
- [28] Mills K C 2002 *Recommended Values of Thermophysical Properties of Selected Commercial Alloys* (Materials Park, OH: ASM)
- [29] Iida T and Guthrie R I L 1988 *The Physical Properties of Liquid Metals* (Oxford: Clarendon)
- [30] Ho C Y and Touloukian Y S 1977 *Thermophysical Properties of Matter: Specific Heat* (TPRC Data Series, Thermophysical Properties Research Centre, Purdue University) (New York: IFI/Plenum)
- [31] James A and Lord M 1992 *VNR Index of Chemical and Physical Data* (New York: Van Nostrand Reinhold)
- [32] Chase M W 1998 *NIST-JANAF Thermochemical Tables* 4th edn (Melville, NY: American Institute of Physics)
- [33] Kaye G W C and Laby T B 1995 *Tables of Physical and Chemical Constants* (London: Longmans)
- [34] Yaws C L 1997 *Handbook of Thermal Conductivity* (Houston: Gulf Publishing)
- [35] Ho C Y and Touloukian Y S 1977 *Thermophysical Properties of Matter: Thermal Conductivity* (TPRC Data Series, Thermophysical Properties Research Centre, Purdue University) (New York: IFI/Plenum)
- [36] Ho C Y, Liley P E, Power R W and National Bureau of Standards 1968 *National Standard Reference Data Series: No. 16: Thermal Conductivity of Selected Materials*, Pt 2 (Washington DC: USGPO)
- [37] Turkdogan E T 1980 *Physical Chemistry of High Temperature Technology* (New York: Academic)
- [38] Mishra S and DebRoy T 2004 *Acta Mater.* **52** 1183–92
- [39] Bird R B, Stewart W E and Lightfoot E N 1960 *Transport Phenomena* (New York: Wiley)
- [40] Patankar S V 1980 *Numerical Heat Transfer and Fluid Flow* (New York: Hemisphere)
- [41] Voller V R and Prakash C 1987 *Int. J. Heat Mass Transfer* **30** 1709–19
- [42] Brent A D, Voller V R and Reid K J 1988 *Numer. Heat Transfer* **13** 297–318
- [43] Zhang W, Kim C H and DebRoy T 2004 *J. Appl. Phys.* **95** 5210–19
- [44] Zhang W, Kim C H and DebRoy T 2004 *J. Appl. Phys.* **95** 5220–9
- [45] Kumar A and DebRoy T 2003 *J. Appl. Phys.* **94** 1267–77
- [46] Kou S and Sun D K 1985 *Metall. Trans. A* **16A** 203–13
- [47] Kim C H, Zhang W and DebRoy T 2003 *J. Appl. Phys.* **94** 2667–79
- [48] He X, Elmer J and DebRoy T 2005 *J. Appl. Phys.* **97** 84909
- [49] He X, DebRoy T and Fuerschbach P 2003 *J. Appl. Phys.* **94** 6949–58
- [50] Elmer J W, Palmer T A, Zhang W, Wood B and DebRoy T 2003 *Acta Mater.* **51** 3333–49
- [51] De A and DebRoy T 2004 *J. Phys. D: Appl. Phys.* **37** 140–50
- [52] De A and DebRoy T 2004 *J. Appl. Phys.* **95** 5230–40
- [53] Greses J, Hilton P A, Barlow C Y and Steen W M 2004 *J. Laser Appl.* **16** 9–15
- [54] Tsubota S, Ishide T, Nayama M, Shimokusu Y and Fukumoto S 2000 *Proc. ICALEO (Dearborn, MI)* C219–225
- [55] Matsunawa A and Ohnawa T 1991 *Trans Japan. Weld. Res. Inst.* **20** 9–15
- [56] Miller R and DebRoy T 1990 *J. Appl. Phys.* **68** 2045–50
- [57] Collur M M and DebRoy T 1989 *Metall. Trans. B* **20B** 277–85
- [58] Wilcox D C 1993 *Turbulence Modeling for CFD* (CA: DCW Industries)
- [59] Launder B E and Spalding D B 1972 *Lectures in Mathematical Models of Turbulence* (London: Academic)
- [60] Hong K 1996 *PhD Thesis* University of Waterloo 145 pp
- [61] Yang Z and DebRoy T 1999 *Metall. Trans. B* **30B** 483–93
- [62] Geiger H and Poirier D R 1973 *Transport Phenomena in Metallurgy* (London: Addison Wesley)
- [63] Rosenthal D 1946 *Trans. ASME* **48** 849–66
- [64] Pastor M, Zhao H, Martukanitz R P and DebRoy T 1999 *Weld. J.* **78** (6) 207s–216s
- [65] Khan P A A and DebRoy T 1984 *Metall. Trans. B* **15** 641–4
- [66] Sahoo P, Collur M M and DebRoy T 1988 *Metall. Trans. B* **19** 967–72